Higher-Order Mesoscopic Self-Assembly of Fluorinated Surfactants on Water Surfaces

Motomu Tanaka, Marie Pierre Krafft, Andreea Pasc

▶ **To cite this version:**

Motomu Tanaka, Marie Pierre Krafft, Andreea Pasc. Higher-Order Mesoscopic Self-Assembly of Fluorinated Surfactants on Water Surfaces. NPG Asia Materials, inPress, 15 (1), pp.23. 10.1038/s41427-023-00466-z . hal-03983642

HAL Id: hal-03983642
https://hal.science/hal-03983642

Submitted on 11 Feb 2023

HAL is a multi-disciplinary open access archive for the deposit and dissemination of scientific research documents, whether they are published or not. The documents may come from teaching and research institutions in France or abroad, or from public or private research centers.

L'archive ouverte pluridisciplinaire **HAL**, est destinée au dépôt et à la diffusion de documents scientifiques de niveau recherche, publiés ou non, émanant des établissements d'enseignement et de recherche français ou étrangers, des laboratoires publics ou privés.

Higher-Order Mesoscopic Self-Assembly of Fluorinated Surfactants on Water Surfaces

Running title: Hierarchical Self-Assembly of Fluorocarbons

Motomu Tanaka[1,2], Marie Pierre Krafft[3], Andreea Pasc[4]

[1] Center for Integrative Medicine and Physics, Institute for Advanced Study, Kyoto University, Kyoto, Japan

[2] Physical Chemistry of Biosystems, Institute of Physical Chemistry, Heidelberg University, Heidelberg, Germany

[3] Institut Charles Sadron (CNRS), University of Strasbourg, Strasbourg, France

[4] University of Lorraine (CNRS), L2CM UMR 7053, F-5400, Nancy, France

Abstract

Surfactants containing fluorocarbon chains have been drawing increasing attentions, because they self-assemble into a variety of microscopic and mesoscopic domains. They tend to form highly ordered patterns at the air/water interface, which are clearly different from those formed by their hydrocarbon analogues. Focusing on fluorinated surfactants possessing unique physical characteristics, this review aims to give an overview how the interplay of line tension and dipole interaction, the comprehensive principle, governs the pattern formation of two-dimensional self-assemblies. This review also covers several key experimental and analytical techniques that are useful for the characterization of the shape, size, correlation, and viscoelasticity of hierarchical self-assemblies on water surfaces. Finally, several biomedical applications, including biomimetic surface coating, multi-modal contrast agents in medical diagnostics, and controlled delivery of

gases (O_2 and NO) for oxygenation and antimicrobial effect, are introduced to highlight how the unique physicochemical properties of fluorinated self-assemblies can be applied in materials science.

Higher-order pattern formation by molecular self-assemblies is a universal phenomena.

A wide range of organic molecules (including surfactants, liquid crystals, and diblock copolymers) have various hierarchical two- and three-dimensional patterns and textures.[1, 2] For example, circular domains, stripes, and chiral crystal structures have been found in Langmuir monolayers of lipids and surfactants at the air/water interface.[3, 4] Three-dimensional lamellae, inversed hexagonal micelles, and bicontinuous cubic phase assemblies of lipids,[5, 6] liquid crystals,[7] and diblock copolymers[8, 9, 10, 11] have been found. Intriguingly, a small set of structural parameters leads to very similar patterns, independent from the detailed molecular structures. For example, Israelachivili, Mitchell, and Ninham theoretically accounted the shape of self-assembled surfactant aggregates using a geometric packing constraint, $p = v/Al$, where v is the volume of hydrophobic core, A is the surface area (area occupied by a head group), and l is the axial length of the surfactant molecule.[12] This simple geometric constraint can be applied to predict the morphology of various supramolecular architectures formed by a wide variety of molecules with different size and structures, including phospholipids, liquid crystals, and block copolymers. On the other hand, the characteristic length scale scale and periodicity of patterns can range over several orders of magnitude, from tens of nanometers (e.g. periodicity of phospholipid "ripples")[13] to hundreds of micrometers (e.g. stationary patterns driven by chemical reactions).[14] As comprehensively summarized by Seul and Andelman from the theoretical viewpoint,[2] these patterns are stabilized through interplay between competing intermolecular interactions characterized by the spatial

variation of order parameters. In two-dimensional assemblies on water surfaces dealt in this review, the competition of line tension and dipole interaction play dominant roles, as described more explicitly in the following sections.

Fluorinated surfactants: what make them unique compared with hydrocarbon analogues?

This review aims to provide a comprehensive overview on the physical principles governing the formation of highly ordered patterns by self-assemblies. As an example, we take fluorinated surfactants that have been shown to form a rich variety of patterns that are distinct from the commonly studied hydrocarbon analogues. Fluorocarbon chains have different structures and physical properties to their hydrocarbon analogues.[15, 16, 17] A fluorine atom is bulkier than a hydrogen atom, so ordered fluorocarbon chains have rigid 15/7 helical conformations rather than all-*trans* conformations as in the case of hydrocarbon chains. The cross-sectional areas of fluorocarbon chains, 27–30 $Å^2$,[18] are therefore larger than the cross-sectional areas of hydrocarbon chains with all-*trans* conformations, 18–21 $Å^2$. The cohesion energy between fluorocarbon chains is lower than the cohesion energy between hydrocarbon chains because fluorocarbon chains are less polarizable than hydrocarbon chains. Moreover, the surface potentials of surfactant fluorocarbon chains at the air/water interface are negative with respect to water,[19, 20] indicating that the molecular dipoles of fluorocarbon chains point in the opposite direction to the molecular dipoles of hydrocarbon chains. Importantly, hydrocarbons and fluorocarbons are both hydrophobic but are totally immiscible, fluorocarbon chains being lipophobic but hydrocarbon chains being fluorophobic.

The clear differences in physico-chemical properties between fluorocarbons and hydrocarbons and their mutual immiscibility suggest that the self-assemblies of compounds containing fluorocarbon

chains should be distinct from those of their hydrocarbon analogues. Kunitake, Ringsdorf, and their co-workers synthesized phospholipids containing fluorocarbon chains and found that these lipids were hardly miscible with lipids containing hydrocarbon chains.[21, 22, 23] Riess et al. synthesized various modular single- and double-chain fluorinated surfactants with polar heads derived from phospholipids, amino-acids, sugars, polyols and other biomaterials and characterized their physicochemical properties.[24, 25] Intriguingly, the compounds containing both fluorocarbon and hydrocarbon chains tend to self-assemble into micelles in either fluorocarbon or hydrocarbon solvents.[26, 27, 28]

"Microstripes" of fluorinated surfactants in the diluted phase: a dipolar monolayer

How will fluorinated surfactants self-assemble when deposited on a water surface? What are the main differences from self-assembly of hydrocarbon analogues? To address these questions, Schneider et al. deposited fully hydrogenated dihexadecylglycerol (diHC16) and its half-fluorinated analogue (diFC8-8) on a water surface.[29] They observed the self-assemblies of diHC16 and diFC8-8 using a Langmuir film balance coupled to an upright fluorescence microscope while determining the pressure–area isotherms.[30] The pressure–area isotherms of diHC16 and diFC8-8 are shown in Figure 1a and 1b, respectively. It can be seen that the area per molecule is higher for diFC8-8 than diHC16 at all surface pressures. At π = 25 mN/m, the area of one diFC8-8 molecule is 57 Å^2 but the area of one diHC16 molecule is 38 Å^2. This is caused by the difference between the cross-sectional areas of a fluorocarbon chain (30 Å^2) and a hydrocarbon chain (19 Å^2) and the diFC8-8 and diHC16 molecules each possessing two chains. Near when the pressure starts to increase, diHC16 has circular "bubble-like" domains at $\pi \approx$ 65 Å^2 (Figure 1a) similar to the ones found for other lipids with hydrocarbon chains.[4] In contrast, diFC8-8 forms micrometer-thick,

"stripe-like" domains at $A \approx 95$ Å^2 (Figure 1b). Both types of microdomain are thermodynamically stable and found in the coexistence of gas and liquid phases. Further compression of either system causes the film to give homogeneous fluorescence signals.

Like for other condensation transitions, the formation of stripe-like domains of diFC8-8 molecules near the first-order phase transition between the gas and liquid phases occurs when attractive interactions between molecules becomes dominant against the mixing entropy. The shapes and thicknesses of stripe-like domains are determined by the competitive interplay between line tension and dipole interactions, as theoretically described by McConnell and Andelman.[31, 32] Free energy of line tension F_{line}, represented by the energy contribution by line tension γ to create phase boundary is linearly proportional to the peripheral length L of the phase boundary, $F_{\text{line}} = \gamma L$. Namely, the line tension favors circular shapes to minimize the free energy, as found for diHC16 and other hydrocarbon-based surfactants. However, the molecular dipole moment tends to stretch isolated domains because of electrostatic interactions. In this scenario, the contribution of the line tension to the domain energy is, $F_{\text{line/stripe}} = \frac{2\gamma}{D}$, where periodicity D is given as the sum of the thicknesses of gas (D_{G}) and liquid (D_{L}) phases, $D = D_G + D_L$.

Previously, Andelman et al. theoretically predicted that the stripe domains are stabilized through density modulation caused by dipole contributions from the head groups.[32, 33] However, this cannot explain the formation of bubble-like domains by diFC8-8 and microstripes by diHC16, because they have identical –OH head groups. Thus, these data suggest that the dipole moments of the chain termini (–CH_3 and –CF_3 groups) as well as those of –CH_2–CF_3– junctions play dominant roles in determining the shape and size of domains. The surface potentials of diFC8-8 and diHC16, determined using the Helmholtz equation $V = \frac{\mu}{\varepsilon A}$ [34], have opposite signs, indicating that the dipole

moment of diFC8-8 points away from the monolayer toward the air,[30] as reported previously.[20, 35] In the Helmholtz equation, μ is the effective dipole moment and A is the area per molecule. Assuming that the infinitely long stripe domains of the gas and liquid phases with thicknesses D_G and D_L, respectively, are separated by sharp boundaries, the free energy of the stripe geometry can be calculated using the following Eq. 1,

$$F = \frac{k_B T b^3}{\pi\sqrt{A}}[x_L\phi_L^2 + x_G\phi_G^2] - \frac{b^3}{\pi D}(\phi_L - \phi_G)^2 \log\left(\frac{D\sin\pi x}{\pi\sqrt{A}}\right), \quad \text{Eq. 1}$$

where x and ϕ are the fraction and surface concentration (mol/m^2) of each phase, $b^3 = \frac{\mu^2\varepsilon}{k_B T\varepsilon_0(\varepsilon+\varepsilon_0)}$, and ε and ε_0 are the dielectric constant near the dipoles and the dielectric constant of water, respectively. The first two terms give the mean contribution of the electrostatic energy and are therefore independent of D, but the third term is the sum of the intra- and inter-stripe dipolar interactions.[36] The difference between the total free energies of the stripe phase and a reference gas–liquid coexistence is therefore

$$\Delta F = \frac{k_B T b^3}{\pi D}(\phi_L - \phi_G)^2 \log\left(\frac{D\sin\pi x}{\pi\sqrt{A}}\right) + \frac{2\gamma}{D}. \quad \text{Eq. 2}$$

Minimizing ΔF with respect to the periodicity D gives the equilibrium stripe width:

$$D_{eq} = \frac{\pi\sqrt{A}}{\sin\pi x}\exp\left[\frac{2\pi\gamma}{k_B T b^3(\phi_L-\phi_G)^2} + 1\right]. \quad \text{Eq. 3}$$

Using the previously reported line tension $\gamma = 1.6 \times 10^{-12}$ N,[37] and the experimentally determined surface area and potential values, the equilibrium thickness $D_{eq} \approx 1$ μm can be calculated using Eq. 3. This equilibrium thickness agrees well with the experimentally determined equilibrium thicknesses D_{exp} = 2–8 μm. Decreasing γ by adding a substitutional impurity like cholesterol resulted in a significant decrease in D_{exp}, which gives supporting evidence that the competition between dipole interactions and line tension determine the periodicity.

Experimental determination of shape, size, and long-range order of self-assembled domains

Krafft et al. synthesized various semi-fluorinated alkanes $C_nF_{2n+1}C_mH_{2m+1}$ (*FnHm* diblocks; Figure 2a)) based on covalent connections between fluorocarbon (*Fn*) and hydrocarbon (*Hm*) segments.[38, 39] These molecules contain no hydrophilic moieties but form stable Langmuir monolayers at the air/water interface.[28, 40] It is well established that hydrocarbon-based surfactants tend to form a flat monolayer, which can be treated as a two-dimensional continuum. In contrast, the atomic force microscopy (AFM) images of *FnHm* monolayers transferred onto solid substrates indicated that a *FnHm* monolayer consists of monodisperse, disk-like domains with diameters of 20–40 nm.[41] The orientation of molecules was initially debated because both moieties are hydrophobic. Abed et al. claimed that antiparallel stacking of diblocks occurs,[42] but X-ray/neutron reflectivity and surface potential measurements indicated that the fluorocarbon chains are in contact with air and the hydrocarbon chains are in contact with water.[43, 44, 45, 46, 47]

A theoretical study[48] demonstrated that the micelles are mesoscipic domains of a high density phase of the *FnHm* molecules taking vertical orientations (the fluorinated segments being extended toward air and the hydrocarbon segments toward water) and the continuous phase is of lower density and the *FnHm* diblocks are nearly parallel to the water surface. As described in the previous section, the shape and size of mesoscopic domains are determined by the competitive interplay between line tension and dipole interactions. Here, the line tension favors coalescence of circular domains to minimize the tension free energy of line tension, $F_{\text{line}} = \gamma L$. On the other hand, the repulsive electrostatic interactions between domains contribute to avoid the coalescence of domains and keep their size distribution monodisperse.

158 Notably, the self-assembled mesoscopic domains act like colloidal particles and assemble into
159 hexagonal arrays. Topographic profiles acquired by AFM demonstrated that the mesoscopic
160 domains of *FnHm* diblocks have long-range order beyond their own sizes. However, once a
161 monolayer has been transferred onto a solid substrate, the domains loose translational and
162 rotational degrees of freedoms. Therefore, it is desired to determine the hierarchical structures of
163 self-assembled semi-fluorinated alkanes on a "free" water surface. Among various surface
164 sensitive techniques, grazing incidence small-angle X-ray scattering (GISAXS) is a powerful tool
165 for determining the long-range correlation between self-assembled mesoscopic objects on the
166 water surface that cannot be visualized by optical microscopy.[49, 50] Fontaine et al. performed
167 GISAXS measurements of *F*8*H*16 monolayers at the air/water interface. At the surface pressure
168 of π = 5 mN, they identified several diffraction peaks that were assigned to a hexagonal lattice
169 with a unit length of 33 nm.[47] Bardin et al. found that the lattice parameter increases monotonically
170 as the hydrocarbon chain length increases, suggesting that subtle changes in molecular structure
171 can be used to change the lattice parameter.[51] On the other hand, it is noteworthy that the lattice
172 parameter does not directly correspond to the domain size, because the discrete domains are
173 separated by the diluted phase. Therefore, quantitative calculations of GISAXS signals are
174 necessary to determine the domain size more precisely.
175 Figure 2b shows the experimental setup and the scattering geometry for GISAXS measurements at
176 the air/water interface. A monolayer of diblocks *FnHm* or tetrablocks di(*FnHm*) is deposited on the
177 Langmuir film balance and compressed to surface pressure π. A monochromic synchrotron beam
178 impinges the interface at incident angle α_i (slightly lower than the critical angle of total reflection),
179 e.g., α_i = 0.12° for 8 keV and α_i = 0.2° for 10 keV, and the scattering signals are detected using a
180 two-dimensional pixel detector. The GISAXS signal for a *F*10*H*16 monolayer is shown in Figure 2c.

The black rectangle near $q_y = 0$ is the direct beam masked by a beam stop. The maximum scattering intensity is $q_z \approx 0.28$ nm^{-1}, called the Yoneda peak. The maximum scattering intensity decreases rapidly as q_z increases. To gain sufficient counting statistics, the signal intensity was integrated between $q_z = 0.7$ and 0.9 nm^{-1} (indicated by white dashed lines), which is sufficiently far from the Yoneda peak and the beam stop. The integrated GISAXS signal is shown in Figure 2d.

The GISAXS signal intensity $I(q_y)$ can generally be determined from the structure factor $S(q_y)$ and form factor $F(q_y)$,

$$I(q_y) = A\left|F(q_y)\right|^2 \cdot S(q_y). \quad \text{Eq. 4}$$

where A is a scaling factor. Form factor $F(q_y)$ reflects the shapes and sizes of the objects, whereas structure factor $S(q_y)$ reflects the lateral organization of the objects. The model used to determine the form factor was selected based on AFM observations. For example, $F(q_y)$ for an oblate hemispheroid with diameter Φ and height H (Figure 2d inset) was used for the *FnHm* domains,[52] using Eq. 5

$$F(q_x, q_y, q_z\, \Phi, H) = 2\pi \int_0^H \left(\frac{\Phi}{2}\right)^2 \left(1 - \left(\frac{z}{H}\right)^2\right) J_1\left(\frac{\Phi\sqrt{(q_x{}^2 + q_y{}^2)\left(1-\left(\frac{z}{H}\right)^2\right)}}{2}\right) exp(-iq_z z)dz. \quad \text{Eq. 5}$$

J_1 is the first-order Bessel function of the first kind. The calculated $F(q_y)$ is shown as a gray line in Figure 2d. However, $F(q_y)$ of an oblate hemiellipsoid was used to give the best fit for di(*FnHm*) tetrablocks.[53] It is notable that form factor should be calculated within the framework of the distorted wave Born approximation (DWBA) that takes the multiple scattering events caused by the beam larger than the objects into account.[54, 55]

The structure factor $S(q_y)$ is modeled in the framework using paracrystal theory. The $S(q_y)$ for *FnHm* is modeled using a two-dimensional hexagonal lattice (the blue line in Figure 2d),[52] as shown in Eqs. 6 and 7,

$$\frac{(1-\varphi^2)^2}{(1+\varphi^2-2\varphi\cos(q_yL))\left(1+\varphi^2-2\varphi\cos\left(\frac{q_yL}{2}+\frac{\sqrt{3}q_xL}{2}\right)\right)}, \quad \text{Eq. 6}$$

where

$$\varphi = \exp\left(\frac{-(q_x^2+q_y^2)\sigma^2}{2}\right)\exp\left(\frac{-L}{\xi}\right). \quad \text{Eq. 7}$$

This gives not only the lattice parameter L and its standard deviation σ but also the correlation length ξ, which cannot be determined from the peak positions. For example, the size and correlation length of *F*10*H*16 domains calculated from the fit are Φ = 30 nm and ξ = 505 nm, respectively, indicating that the correlation between hemispherical *F*10*H*16 domains can reach over the distance that is more than 15 times larger than the domain diameter. As shown in the green line in Figure 2d, the combination of $F(q_y)$ and $S(q_y)$ shows excellent agreement with the experimental data. On the other hand, $S(q_y)$ for di(*FnHm*) was modeled using an orthorhombic (distorted hexagonal) paracrystal lattice.[53] The best model for each system was selected by checking for agreement between the global shape of the GISAXS signals and peak positions using several candidate models. Yet, the use of GISAXS technique to mesoscopic self-assemblies of small organic molecules is still technically nontrivial for several reasons. The signals can be smeared if the domain size distribution is broad. Moreover, one should take care about the trade-off between the signal intensity (counting statistics) vs. radiation damage. Nevertheless, GISAXS is an emerging technique that opened a large potential for identifying the shapes, sizes, and long-range orders of mesoscale self-assemblies of organic molecules that form on water surfaces that cannot be identified otherwise.

Mechanical interactions between self-assembled domains: formation of physical gels

Another remarkable characteristic of fluorocarbon surfactants and semi-fluorinated alkanes at the air/water interface is that a monolayer is very poorly compressible. Maaloum et al. found that the

domain structures in films transferred onto solid substrates at $\pi \geq 0.5$ mN/m suggested that *FnHm* molecules self-assemble into mesoscopic domains even without compression.[41] In fact, the onset of surface pressure increase is immediately followed by a steep increase with very small decrease in area. The isothermal compressibility χ of a *FnHm* monolayer at $\pi = 5$ mN/m, $\chi = -\frac{1}{A}\left(\frac{\partial A}{\partial \pi}\right) \approx 10$ m/N, is as low as the isothermal compressibility of a fatty acid in a highly condensed state.[56] In fact, the domain size Φ and the Φ/L ratio of a *FnHm* determined by GISAXS are remarkably independent of π.[52]

These findings suggest that the self-assembled, mesoscopic domains of *FnHm* establish long-range correlation at a very low π. To quantify the significance of mechanical interactions between the domains, several research groups have measured the interfacial viscoelasticity of *FnHm* monolayers. Klein et al. used an interface stress rheometer based on a gliding magnetic needle under oscillating magnetic fields[57] and reported that *F*12*H*12 and *F*12*H*20 monolayers are predominantly elastic.[58] Veschgini et al. used another type of interfacial stress rheometer based on a rotating ring coupled to a Langmuir film balance (Figure 3a).[59] In this system, an oscillatory shear stress is applied to the monolayer by rotating the ring at frequency ω and driving amplitude γ. The amplitude and phase shift of the ring are used to determine the dynamic surface modulus $G^*(\omega) = G'(\omega) + iG''(\omega)$ as a complex function of ω. The real part, the shear storage modulus *G*' is a measure of the elastic properties, while the imaginary part the shear loss modulus *G*" is a measure of the viscous properties.

The storage (G') and loss (G'') moduli of a *F*8*H*16 monolayer are plotted against the area per molecule *A* in Figure 3b. G' and G'' start increasing at $A \approx 50$ Å^2 but the surface pressure remains $\pi \approx 0$ mN/m (inset). G' is always larger than G'', indicating that the *F*8*H*16 monolayer is predominantly elastic. This behavior, the formation of two-dimensional gels even in a highly

diluted phase, is distinct from two-dimensional gelation of other surfactant monolayers that occurs only at a high surface pressure for the formation of hydrogen bonds or through cross-linking via entanglement for denatured proteins.[59, 60, 61] The unique viscoelastic properties of *FnHm* and di(*FnHm*) can be attributed to strong dipole repulsion between CF_3 chain termini and CF_2–CH_2 junctions preventing the coalescence of surface domains. The systematic variation of the lengths of *Fn* and *Hm* blocks, indicate that the elongation of the *Fn* block from 8 to 12 units increased G' by almost an order of magnitude but elongating the *Hm* block did not change G' as much.[56] Genzer et al.[62] found that increasing ordering in the "bulkier" fluorocarbon chain by elongating the chain from $n = 10$ to 12 does not disturb the lateral packing of hydrocarbon chains. The marked increase in *G'* caused by elongating the *Fn* block can be attributed to the increase in domain size due to a higher alignment of the molecular dipoles.[30, 52] Figure 3c shows the frequency dispersion of *G*' and *G*" of *F*8*H*18 monolayers measured under a slight variation of area per molecule; 50 Å^2 ($\pi = 0$ mN/m), 40 Å^2 ($\pi = 0$ mN/m), 33 Å^2 ($\pi = 1$ mN/m), and 31 Å^2 ($\pi = 8$ mN/m). At a surface pressure of zero ($A = 50$ and 40 Å^2), the power law exponents in the double logarithmic plots for both G' and G'' are ≈ 1, which is a characteristic of a soft glassy material.[63, 64] Intriguingly, the exponents of *G*' become zero as soon as the surface pressure becomes positive but the G'' exponents remain constant at ≈ 1. The observed frequency dispersions at $\pi > 0$, $G' \propto f^0$ and $G'' \propto f^1$, are typical for a classical Kelvin–Voigt solid.[65] When one plots *G*" versus *G*' (Figure 3d), the film behaves predominantly elastic over the whole frequency window at $\pi = 0$ mN/m ($G' < G''$) and the phase shift δ remains at ≈ 0.6 (inset). In contrast, once the film was slightly compressed to $\pi > 0$ mN/m (open symbols), δ shows an increase with increasing frequency f to the region where the film becomes predominantly viscous ($\delta > \pi/2$, *G*" > *G*') beyond a critical frequency. The formation of two-dimensional physical gels through mesoscopic domains of *FnHm* diblocks even at $\pi = 0$ mN/m

shares common features with the formation of gels from "hard" particles but has not previously been found for self-assembled films of small organic molecules. These rheological properties can be attributed to strong dipole repulsion between *FnHm* domains.

Higher-order self-assembly in lipid membranes

Sphingolipids, cholesterol, and phospholipids in biological cell membranes form laterally organized functional domains called "rafts".[66] Ample evidence has shown that mesoscopic/microscopic domains play key roles in complex cellular functions because spatial confinement of functional molecules allows fine-tuning of cooperative polyvalent interactions between biomolecules.[67] Many studies showed the formation of raft-like domains by the self-assembly of "raft-like" lipid mixtures [68], but most of them are either polydisperse in size or coalescing into large domains due to line tension. As described above, using lipids containing fluorocarbon chains is a promising strategy to avoid the tension-driven coalescence of domains.

The total free energy F_{total} of a membrane containing domains with diameter D can be described as the sum of the electrostatic energy F_{el} and tension energy F_{λ}[31] using Eqs. 8–10,

$$F_{\text{total}} = F_{\text{el}} + F_{\lambda}, \quad \text{Eq. 8}$$

where

$$F_{\text{el}} = \pi D(\Delta m)^2 \ln\left(\frac{e^2\delta}{4R}\right), \quad \text{Eq. 9}$$

and

$$F_{\lambda} = \pi D\lambda. \quad \text{Eq. 10}$$

Δm is the difference between the molecular dipole densities of the lipids in the domains and the matrix lipids, δ is the dipole–dipole distance at the phase boundary, and e is Euler's constant. The

line tension λ contains the mismatch between the surface tension $\Delta\gamma$ and the molecular length Δl, $\lambda = \Delta\gamma \cdot l + \gamma \cdot \Delta l$. Minimizing the yields therefore gives the equilibrium domain diameter D_{eq},

$$D_{\mathrm{eq}} = \left(\frac{e^3\delta}{8}\right) exp\left(\frac{\lambda}{\Delta m^2}\right). \quad \text{Eq. 11}$$

D_{eq} can be calculated because all of the parameters required for the calculation can be determined experimentally. This suggests that the domain size can be changed by a subtle change in the lengths and densities of the fluorocarbon chains.

Pasc et al. synthesized lipids with perfluorinated anchors (FLn; Figure 4a) and mixed them with phospholipids with hydrocarbon chains such as dioleoylphosphatidylcholine (DOPC).[69, 70] Fluorescence images of DOPC monolayers incorporating FL10, FL13, and FL17 domains at molar fractions χ of 0.10, 0.20, and 0.33 are shown in Figure 4b. The domains are round and uniform, showing no sign of coalescence even at a high χ value. The calculated D_{eq} values (T) and experimentally determined domain size D (E) are shown in Figure 4c. It can be seen that the results agree well as the fluorocarbon chain is elongated, so increasing n leads to a marked decrease in the domain size.[70] The size of the FL17 domains was close to the optical microscope resolution ($D \approx 0.3$ μm), which was also precisely determined by grazing incidence X-ray diffraction using a Si (111) analyzer crystal.[69] Like other colloidal self-assemblies in different length scales,[71, 72] the long-range correlation between FLn domains can be assessed by calculating the potential of mean force $V(r)$ within the framework of inverse work function theorem using Eq. 12

$$V(r) \sim -k_B T \ln g(r), \quad \text{Eq. 12}$$

where $g(r)$ is the radial distribution function

$$g(r) = \frac{dN(r+dr)}{d(A+dA)} \cdot \frac{N}{A}. \quad \text{Eq. 13}$$

Figure 4d shows $-\frac{V(r)}{k_BT}$ plotted as a function of r for FL10, FL13, and FL17 at χ = 0.33. The position of the first minimum in each curve coincides with the mean center-to-center distance between the nearest neighbors and monotonically decreases as n increases. The potential near the first minimum can be approximated well as a harmonic potential (red line), and the significance of inter-domain correlation can be evaluated by the second derivative of the potential that is nothing but a spring constant for the potential confinement. The spring constant increases by an order of magnitude as the fluorocarbon chain length increases from n = 10 to 17, indicating that the smaller FLn domains are confined in steeper potential wells than the larger FLn domains. Intriguingly, the FL17 domains have distinct minima up to the third order, indicating that the relationships between domains can reach more than an order of magnitude further than the size of a single domain. As expected, the spring constant decreases as χ decreases and uncorrelated interactions following the Yukawa potential[73] occur at $\chi < 0.05$.[70] More recently, Nakahata et al. demonstrated that the tetrablock di(F10H16) incorporated into a dipalmitoylphosphatidylcholine (DPPC) monolayer affects the lateral organization of DPPC, resulting in large, complex flower-like patterns using fluorescence and Brewster angle microscopy.[74]

Higher-order self-assembly for biomimetic coating materials

From the biomaterial science viewpoint, adding functionalities to highly ordered meso-/micro-domains of fluorinated lipids embedded in lipid membranes could allow the lipid membranes to act as surrogate surface coatings containing ligand molecules confined in defined, discrete domains. This offers advantages over commonly used surrogate surfaces for studying the adhesive functions of cells. For example, confluent cell monolayers such as monolayers of epithelial cells cannot distinguish between the roles of different ligand-receptor pairs because cells contain complex

mixtures of ligand molecules. A surrogate surface based on a supported membrane will allow the surface to be functionalized at precisely controlled inter-ligand densities, but the distribution of functional moieties on the surface is uniform unless a phase-separated membrane is used. However, as described above, the domains of lipid mixtures containing only hydrocarbon chains tend to coalesce due to line tension, resulting in domains with sizes comparable to or even larger than a cell.

Kaindl et al. chemically attached simple mannose to the head group of FL10 (FL10Man; Figure 5a) and investigated how discrete ligand confinement affects adhesion of macrophage-expressing mannose receptor, which is a 180 kDa C-type lectin containing multiple mannose binding units.[75] Macrophages use multivalent mannose receptor interactions to capture and internalize various mannose-containing proteins.[75, 76] A fluorescence image and the potential of mean force for FL10Man at $\chi = 0.33$ are shown in Figure 5b. It can be seen that FL10Man forms uniform and highly ordered domains like FL10 (Figure 4b), showing no sign of coalescence. This provides clear proof that dipole repulsion between fluorocarbon chains but not between head groups plays a dominant role in preventing coalescence of self-assembled lipid domains. Confocal fluorescence images and microinterferometry images of a murine macrophage adhered to glass substrates coated with three types of lipid membranes are shown in Figure 5c. Most of the cells in contact with pure phospholipid (DOPC) membranes could be removed even by a gentle medium exchange. The three-dimensional reconstructed confocal image of a cell shown in the upper left panel of Figure 5c suggests that the cell is hardly deformed and retains its original ellipsoid shape. The microinterferometry image (lower left of Figure 5c) indicates that very little cell–substrate contact occurred (the relevant area is indicated with a yellow line for clarity), indicating almost negligible non-specific cell adhesion to a pure phospholipid membrane. In contrast, when the same

362 macrophages are in contact with the substrate coated with a membrane only consisting of
363 FL10Man (χ = 1.0), the cells were markedly deformed and spread all over the substrate (upper
364 middle part of Figure 5c). The cell–surface contact area shown as a dark area in the
365 microinterferometry image (lower middle part of Figure 5c) is uniform, indicating that the bottom
366 surfaces of the cells adhere uniformly to the membrane-coated substrate. As shown in the upper
367 right image in Figure 5c, macrophages adhere to and spread on the membrane-displaying domains
368 of FL10Man (χ = 0.33) and extend thin lamellipodia to the surrounding areas. Intriguingly, the
369 adhesion zones visualized by microinterferometry contained uniform dark spots (lower right part
370 of Figure 5c) with comparable sizes to the FL10Mon domains (Figure 5b). During the initial
371 spreading process, the spreading front repeatedly stick and advance rather than continually
372 propagated, indicating that the cells find discrete contact points when they are in contact with a
373 new environment. A membrane containing discrete functionalized fluorinated lipid domains could
374 also be used as a coating for a coverless microfluidic channel on which the medium is driven by a
375 surface acoustic wave[77] but not by a pump to investigate dynamic adhesion of bacteria onto
376 mannose-functionalized domains (Figure 5d).[78] As these meso-/micro-domains are formed via
377 self-assembly in the aqueous phase, the domains expressing more complex oligosaccharide
378 moieties can easily be reconstituted in cell-sized, giant lipid vesicles without printing or pre-
379 patterning (Figure 5f).[29]
380
381 **Higher order self-assembly for medical applications**

382 Hierarchically organized self-assemblies of fluorinated molecules have been drawing increasing
383 attentions for medical applications. Various types of supramolecular formulations including gels,
384 vesicles, emulsions, microbubbles, and phase-shift emulsions have been designed as contrast

385 agents for multimodal diagnosis, delivery of energy, delivery of oxygen, nitric oxide and other
386 gases, drugs and biomarkers.[16, 79, 80] The few recent examples discussed below illustrate the role
387 of such self-assemblies in diagnosis and therapy.
388 Commercial microbubbles currently used for ultrasound diagnostics are coated with shells made
389 of lipids or albumin, but increasing the control over microbubble size and stability characteristics
390 is a sought after challenge. Among various lipids, DPPC is comonly chosen because they are in
391 mechanically stable liquid condensed phase at 37 °C.[41] Microbubbles consisting of phospholipids
392 and self-assembled fluorinated compounds have been applied for the medical imaging and
393 therapeutic treatment, because the addition of fluorinated compounds increased the life time of
394 microbubbles.[79] It is notable that pure *FnHm* monolayers tend to collapse under a slight decrease
395 in the surface area due to a poor compressibility originating from the strong dipole repulsions.[56]
396 As the quantitative measurements of structure and viscoelasticity of *FnHm* domains in
397 phospholipid microbubbles are technically not possible, Mielke et al. measured the viscielasticity
398 of the mixed monolayers of DPPC and diblocks *FnHm* using dilational rheometer.[81] The use of a
399 monolayer at the liquid/gas interface can be considered as a well-defined mechanical model of
400 microbubbles, because the film thickness (≈ 3 nm) is much smaller than the size of microbubbles
401 (~ 1 μm). Although individual *FnHm* domains cannot be visualized by optical microscopy, they
402 accumulate at the boundary of liquid expanded and liquid condensed phases of DPPC.[41] The
403 *FnHm*-DPPC monolayers exhibited viscoelastic properties comparable to those of phospholipid
404 monolayers and persisted under a larger strain under which a pure *F*8*H*16 monolayer collapsed.
405 Therefore, the mixing of *FnHm* with phospholipid matrix is a promising strategy to improve the
406 bubble stability.

More advanced formulations involve the incorporation of iron oxide nanoparticles in phospholipid microbubbles for the bimodal ultrasound/MRI contrast agents. This can be realized by coating nanoparticles with amphiphilic bisphosphonate dendrons bearing three oligo(ethylene glycol) chains terminated with $-C_2F_5$ or $-C_4F_9$ groups (Figure 6a). The presence of perfluoroalkyl terminal groups was essential to achieve a high stability, because the nanoparticles coated with fluorinated dendrons are located inside the interfacial film, while those bearing hydrocarbon dendrons remain on the surface.[82]

An increasing number of studies have shown that the presence of a fluorocarbon in the gas phase modulates the molecular self-assembly at the gas/liquid interface and enhances the stability of microbubbles significantly. For example, perfluorohexane (*F*-hexane) leads to an increase in the compressibility of pure *FnHm* monolayers by adsorbing to the gas/liquid interface.[83] Moreover, *F*-hexane-enriched gas phase facilitated the displacement of albumin by DPPC at the gas/water interface under periodic deformations mimicking respiration,[84] suggesting that the presence of fluorocarbon gas inside microbubbles is a promising strategy for the formulation of lung surfactant substitutes. As shown in Figure 6b, the hypoxia biomarker EF5 that is connected to a $-C_2F_5$ group is readily incorporated from the aqueous phase into DPPC microbubbles, whose interior is enriched with *F*-hexane.[85] In contrast, EF5 remained in the aqueous phase when the bubble is filled with air. This effective and stable recruitment of EF5$-C_2F_5$ in the presence of *F*-hexane can be explained by the attractive interactions between the C_2F_5 moiety and *F*-hexane. Interestingly, the fluorine-functionalized molecules were shown to partly remain trapped in the DPPC monolayer even after the removal of fluorocarbon gas.[86]

As shown in Figure 6c, the self-assembly of oleophobic fluoroalkyl moieties can further be used to design even more complex composite nanomaterials by coating graphene oxide (GO) or

oxidized single-walled carbon "nanohorn" with the layers of (i) fluorinated dendrimer (*F*-DEN) and (ii) fluorinated poly(ethylene glycol) (*F*-PEG).[87] The various components/building blocks contribute additively to O_2 adsorption, and the highest O_2-loading capacity was attained by the combination of nanohorns coated with *F*-DEN and *F*-PEG. O_2 first adsorbs on the outer *F*-PEG shell, penetrates into the middle *F*-DEN region, and eventually reaches the nanohorn core. The irradiation with a light-emitting diode produced singlet oxygen, $^1O_2$, which can be used for oxygen-dependent (e.g. photodynamic) therapy of cancer as well as for fighting bacteria and viruses through $^1O_2$ generation. A similar formulation built from *F*-DEN, *F*-PEG and nitrogen-doped carbon nanohorns were devised for efficient nitric oxide delivery utilizing the concentric organization.[88]

Summary and perspectives

The general physical principle stabilizing various self-assembled patterns of domains is the interplay between competing intermolecular interactions. On two-dimensional water surfaces, the competition of line tension and dipole interaction plays key roles. This review puts a special focus on fluorinated surfactants that form unique patterns of self-assembled domains at the air/water interface. These patterns, ranging from periodic micrometer-wide stripes to highly correlated mesoscopic hemi-ellipsoids, are clearly different from those formed by their hydrocarbon analogues. In contrast to the domains of hydrocarbon surfactants, the fluorocarbon domains do not coalesce by compression, indicating the dipole repulsion dominates the line tension in the free energy minimization. As demonstrated by the quantitative GISAXS analysis, the shape, size, and lateral correlation between mesoscopic domains are modulated by subtle changes in molecular structures, such as the lengths of fluorocarbon- and hydrocarbon chains. Notably, the correlation

between mesoscopic domains can reach over the distance that is one order of magnitude larger than the domain diameter. Such repulsive, long-range interactions between domains also affect the mechanical properties of fluorinated surfactant layers significantly. Interfacial shear rheology experiments revealed that the monolayers of semifluorinated diblocks form two-dimensional physical gels even at zero surface pressure. This is clearly different from surfactants with hydrocarbon chains that become predominantly elastic only at high surface pressures.

The unique physical principle of self-assembly and pattern formation by fluorinated surfactants open a wide range of biomedical applications. For example, the addition of biofunctional units enables to confine ligand molecules in discrete areas, which can readily be transferred to the surface of solid substrates or micro-fluidic channels. The substrates displaying highly ordered functional mesostructures are ideally suited to study multivalent, cooperative interactions in biological systems, such as cell adhesion caused by multivalent carbohydrate-protein interactions. As discussed in the last section, a wide variety of supramolecular self-assemblies including gels, vesicles, emulsions, and microbubbles have been formulated for numerous medical applications, including ultrasound/MRI diagnosis, delivery of medical gases such as O_2 and NO, as well as the delivery of drugs and biomarkers. The use of self-assembly in the aqueous phase allows for the integration of mesoscopic domains not only into flat substrates but also into three-dimensional micells and cell-sized vesicles, which cannot be achieved by covalent coupling, printing, or patterning techniques.

Acknowledgments

M.T. thanks D. Andelman (Tel Aviv), C. Gege and R.R. Schmidt (Konstanz), O. Konovalov (ESRF), A. Wixforth (Augsburg), U. Engel (Nikon Imaging Center Heidelberg), and K. Yoshikawa (Kyoto) for fruitful collaboration. M.T. also thanks current and past lab members (S. Mielke, M. Veschgini, T. Kaindl, J. Oelke, M. Schneider, and W. Abuillan) who contributed to the studies described in this review. M.P.K. thanks the CNRS start-up Superbranche (D. Felder-Flesch, Strasbourg) and T. Imae (Taipei) for rewarding cooperation, and Véronique Gouverneur's group (Oxford) for the synthesis of the fluorinated biomarkers. MPK also acknowledges the lab members (N. Nguyen, G. Yang, X. Liu, D. Shi, J. Wallyn, E. Mendoza, and C. Counil) involved in the studies described in this review. The works presented in this review were supported by the JSPS (grant no. JP19H05719 to MT), the German Science Foundation grant no. Ta259/12 (to MT), a German Excellence Strategy grant no. 2082/1-390761711 (to MT), grant ANR-14-CE35-0028-01 (to MPK), the INTERREG V Upper Rhine Program "NANOTRANSMED" (to MPK and MT), and the EU FP7, REA grant agreement no. 606713 BIBAFOODS (to AP and MT). A.P. thanks European Regional Development Funds (FEDER-FSE Lorraine et Massif des Vosges 2014-2020/"Fire Light" project". M.T. thanks the Nakatani Foundation for support. We thank Edanz (https://jp.edanz.com/ac) for editing a draft of this manuscript.

Conflict of Interests

The authors declare that there is no conflict of financial interests in relation to the works described in this review article.

References

1. Witten TA. Structured Fluids. *Physics Today* 1990, **43**(7)**:** 21-28.

2. Seul M, Andelman D. Domain Shapes and Patterns: The Phenomenology of Modulated Phases. *Science* 1995, **267**(5197)**:** 476-483.

3. Weis RM, McConnell HM. Two-dimensional chiral crystals of phospholipid. *Nature* 1984, **310**(5972)**:** 47-49.

4. Möhwald H. Chapter 4 - Phospholipid Monolayers. In: Lipowsky R, Sackmann E (eds). *Handbook of Biological Physics*, vol. 1. North-Holland, 1995, pp 161-211.

5. Luzzati V, Tardieu A, Gulik-Krzywicki T, Rivas E, Reiss-Husson F. Structure of the Cubic Phases of Lipid–Water Systems. *Nature* 1968, **220**(5166)**:** 485-488.

6. Larsson K. Cubic lipid-water phases: structures and biomembrane aspects. *The Journal of Physical Chemistry* 1989, **93**(21)**:** 7304-7314.

7. Kato T. Self-Assembly of Phase-Segregated Liquid Crystal Structures. *Science* 2002, **295**(5564)**:** 2414-2418.

8. Tanaka H, Hasegawa H, Hashimoto T. Ordered structure in mixtures of a block copolymer and homopolymers. 1. Solubilization of low molecular weight homopolymers. *Macromolecules* 1991, **24**(1)**:** 240-251.

9. Bates FS, Schulz MF, Khandpur AK, Förster S, Rosedale JH, Almdal K*, et al.* Fluctuations, conformational asymmetry and block copolymer phase behaviour. *Faraday Discussions* 1994, **98**(0)**:** 7-18.

10. Alexandridis P, Olsson U, Lindman B. A Record Nine Different Phases (Four Cubic, Two Hexagonal, and One Lamellar Lyotropic Liquid Crystalline and Two Micellar Solutions) in a Ternary Isothermal System of an Amphiphilic Block Copolymer and Selective Solvents (Water and Oil). *Langmuir* 1998, **14**(10)**:** 2627-2638.

11. Blanazs A, Ryan AJ, Armes SP. Predictive Phase Diagrams for RAFT Aqueous Dispersion Polymerization: Effect of Block Copolymer Composition, Molecular Weight, and Copolymer Concentration. *Macromolecules* 2012, **45**(12)**:** 5099-5107.

12. Israelachvili JN, Mitchell DJ, Ninham BW. Theory of self-assembly of hydrocarbon amphiphiles into micelles and bilayers. *Journal of the Chemical Society, Faraday Transactions 2: Molecular and Chemical Physics* 1976, **72**(0)**:** 1525-1568.

13. Zasadzinski JAN, Schneir J, Gurley J, Elings V, Hansma PK. Scanning Tunneling Microscopy of Freeze-Fracture Replicas of Biomembranes. *Science* 1988, **239**(4843)**:** 1013-1015.

14. Ouyang Q, Swinney HL. Transition from a uniform state to hexagonal and striped Turing patterns. *Nature* 1991, **352**(6336)**:** 610-612.

15. Banks RE, Smart BE, Tatlow JC (eds). *Organofluorine Chemistry: Principles and Commercial Applications*. Plenum Press: New York, 1994.

16. Riess JG, Cornélus C, Follana R, Krafft MP, Mahé AM, Postel M*, et al.* Novel fluorocarbon-based injectable oxygen-carrying formulations with long-term room-temperature storage stability. *Adv Exp Med Biol* 1994, **345:** 227-234.

17. Krafft MP, Riess JG. Selected physicochemical aspects of poly- and perfluoroalkylated substances relevant to performance, environment and sustainability-Part one. *Chemosphere* 2015, **129:** 4-19.

18. Bunn C, Howells E. Structures of molecules and crystals of fluoro-carbons. *Nature* 1954, **174**(4429)**:** 549-551.

19. Vogel V, Möbius D. Hydrated polar groups in lipid monolayers: Effective local dipole moments and dielectric properties. *Thin Solid Films* 1988, **159**(1)**:** 73-81.

20. Miller A, Helm CA, #xf6, hwald H. The colloidal nature of phospholipid monolayers. *J Phys France* 1987, **48**(4)**:** 693-701.

21. Kunitake T, Okahata Y, Yasunami S. Formation and enhanced stability of fluoroalkyl bilayer membranes. *Journal of the American Chemical Society* 1982, **104**(20)**:** 5547-5549.

22. Higashi N, Kunitake T, Kajiyama T. Surface-Structure and Oxygen Permeation in Mixed Multibilayer Films of Hydrocarbon and Fluorocarbon Amphiphiles. *Macromolecules* 1986, **19**(5)**:** 1362-1366.

23. Ringsdorf H, Schlarb B, Venzmer J. Molecular architecture and function of polymeric oriented systems: models for the study of organization, surface recognition, and dynamics of biomembranes. *Angew Chem Int Ed Engl* 1988, **27:** 113-158.

24. Riess JG, Krafft MP. Fluorocarbons and fluorosurfactants for in vivo oxygen transport (blood substitutes), imaging, and drug delivery. *MRS Bull* 1999, **24:** 42-48.

25. Riess JG. Fluorous micro- and nanophases with a biomedical perspective. *Tetrahedron* 2002, **58:** 4113-4131.

26. Broniatowski M, Dynarowicz-Łątka P. Semifluorinated alkanes — Primitive surfactants of fascinating properties. *Advances in Colloid and Interface Science* 2008, **138**(2)**:** 63-83.

27. Krafft MP. Large organized surface domains self-assembled from nonpolar amphiphiles. *Accounts of Chemical Research* 2012, **45**(4)**:** 514-524.

28. Krafft MP, Riess JG. Chemistry, physical chemistry, and uses of molecular fluorocarbon−hydrocarbon diblocks, triblocks, and related compounds ☒ unique “apolar” components for self-assembled colloid and interface engineering. *Chemical reviews* 2009, **109**(5)**:** 1714-1792.

29. Gege C, Schneider MF, Schumacher G, Limozin L, Rothe U, Bendas G*, et al.* Functional microdomains of glycolipids with partially fluorinated membrane anchors: Impact on cell adhesion. *ChemPhysChem* 2004, **5**(2)**:** 216-224.

30. Schneider MF, Andelman D, Tanaka M. Stripes of partially fluorinated alkyl chains: dipolar Langmuir monolayers. *The Journal of chemical physics* 2005, **122**(9)**:** 094717.

31. McConnell HM. Structures and Transitions in Lipid Monolayers at the Air-Water Interface. *Annual Review of Physical Chemistry* 1991, **42**(1)**:** 171-195.

32. Andelman D, Brochard F, Joanny J-F. Modulated structures and competing interactions in amphiphilic monolayers. *Proceedings of the National Academy of Sciences* 1987, **84**(14)**:** 4717-4718.

33. Andelman D, Broçhard F, Joanny JF. Phase transitions in Langmuir monolayers of polar molecules. *The Journal of Chemical Physics* 1987, **86**(6)**:** 3673-3681.

34. Brockman H. Dipole potential of lipid membranes. *Chemistry and physics of lipids* 1994, **73**(1-2)**:** 57-79.

35. Smondyrev A, Berkowitz M. Molecular dynamics simulation of fluorination effects on a phospholipid bilayer. *The Journal of chemical physics* 1999, **111**(21)**:** 9864-9870.

36. Keller D, McConnell H, Moy V. Theory of superstructures in lipid monolayer phase transitions. *The Journal of Physical Chemistry* 1986, **90**(11)**:** 2311-2315.

37. Benvegnu DJ, McConnell HM. Line tension between liquid domains in lipid monolayers. *The Journal of Physical Chemistry* 1992, **96**(16)**:** 6820-6824.

624 38. de Gracia Lux C, Gallani J-L, Waton G, Krafft MP. Compression of self-assembled nano-
625 objects - 2D/3D transitions in films of (perfluoroalkyl)alkanes - Persistence of an organized
626 array of surface micelles. *Chem Eur J* 2010, **16:** 7186-7198

627
628 39. de Gracia Lux C, Krafft MP. Non-polar gemini amphiphiles self-assemble into stacked
629 layers of nano-objects. *Chem Eur J* 2010, **16:** 11539-11542.

630
631 40. Gaines GL. Surface activity of semifluorinated alkanes: $F(CF_2)m(CH_2)nH$. *Langmuir* 1991,
632 **7:** 3054-3056.

633
634 41. Maaloum M, Muller P, Krafft MP. Monodisperse surface micelles of nonpolar amphiphiles
635 in Langmuir monolayers. *Angewandte Chemie* 2002, **114**(22)**:** 4507-4510.

636
637 42. Abed AE, Fauré MC, Pouzet E, Abillon O. Experimental evidence for an original two-
638 dimensional phase structure: An antiparallel semifluorinated monolayer at the air-water
639 interface. *Physical Review E* 2002, **65**(5)**:** 051603.

640
641 43. Huang Z, Acero AA, Lei N, Rice SA, Zhang Z, Schlossman ML. Structural studies of
642 semifluorinated hydrocarbon monolayers at the air/water interface. *Journal of the*
643 *Chemical Society, Faraday Transactions* 1996, **92**(4)**:** 545-552.

644
645 44. Broniatowski M, Miñones Jr J, Dynarowicz-Łątka P. Semifluorinated chains in 2D-
646 (perfluorododecyl)-alkanes at the air/water interface. *Journal of Colloid and Interface*
647 *Science* 2004, **279**(2)**:** 552-558.

648
649 45. Mourran A, Tartsch B, Gallyamov M, Magonov S, Lambreva D, Ostrovskii BI*, et al.* Self-
650 Assembly of the Perfluoroalkyl-Alkane F14H20 in Ultrathin Films. *Langmuir* 2005, **21**(6)**:**
651 2308-2316.

652
653 46. de Viguerie L, Keller R, Jonas U, Berger R, Clark CG, Klein CO*, et al.* Effect of the
654 Molecular Structure on the Hierarchical Self-Assembly of Semifluorinated Alkanes at the
655 Air/Water Interface. *Langmuir* 2011, **27**(14)**:** 8776-8786.

656
657 47. Fontaine P, Goldmann M, Muller P, Fauré M-C, Konovalov O, Krafft MP. Direct Evidence
658 for Highly Organized Networks of Circular Surface Micelles of Surfactant at the Air−Water
659 Interface. *Journal of the American Chemical Society* 2005, **127**(2)**:** 512-513.

660
661 48. Semenov AN, Gonzàlez-Pérez A, Krafft MP, Legrand J-F. Theory of surface micelles of
662 semifluorinated alkanes. *Langmuir* 2006, **22:** 8703-8717.

663
664 49. Als-Nielsen J. Refraction and reflection from interfaces. *Elements of Modern X‐ray*
665 *Physics*, 2011, pp 69-112.

666

50. Schultz DG, Lin X-M, Li D, Gebhardt J, Meron M, Viccaro J*, et al.* Structure, Wrinkling, and Reversibility of Langmuir Monolayers of Gold Nanoparticles. *The Journal of Physical Chemistry B* 2006, **110**(48)**:** 24522-24529.

51. Bardin L, Fauré M-C, Limagne D, Chevallard C, Konovalov O, Filipe EJM*, et al.* Long-Range Nanometer-Scale Organization of Semifluorinated Alkane Monolayers at the Air/Water Interface. *Langmuir* 2011, **27**(22)**:** 13497-13505.

52. Veschgini M, Abuillan W, Inoue S, Yamamoto A, Mielke S, Liu X*, et al.* Size, Shape, and Lateral Correlation of Highly Uniform, Mesoscopic, Self-Assembled Domains of Fluorocarbon–Hydrocarbon Diblocks at the Air/Water Interface: A GISAXS Study. *ChemPhysChem* 2017, **18**(19)**:** 2791-2798.

53. Abuillan W, Veschgini M, Mielke S, Yamamoto A, Liu X, Konovalov O*, et al.* Long-Range Lateral Correlation between Self-Assembled Domains of Fluorocarbon-Hydrocarbon Tetrablocks by Quantitative GISAXS. *ChemPhysChem* 2019, **20**(6)**:** 898-904.

54. Sinha SK, Sirota EB, Garoff S, Stanley HB. X-Ray and Neutron-Scattering from Rough Surfaces. *Physical Review B* 1988, **38**(4)**:** 2297-2311.

55. Rauscher M, Salditt T, Spohn H. Small-angle x-ray scattering under grazing incidence: The cross section in the distorted-wave Born approximation. *Physical Review B* 1995, **52**(23)**:** 16855-16863.

56. Veschgini M, Habe T, Mielke S, Inoue S, Liu X, Krafft MP*, et al.* Existence of Two-Dimensional Physical Gels even at Zero Surface Pressure at the Air/Water Interface: Rheology of Self-Assembled Domains of Small Molecules. *Angewandte Chemie International Edition* 2017, **56**(41)**:** 12603-12607.

57. Brooks CF, Fuller GG, Frank CW, Robertson CR. An interfacial stress rheometer to study rheological transitions in monolayers at the air− water interface. *Langmuir* 1999, **15**(7)**:** 2450-2459.

58. Klein CO, de Viguerie L, Christopoulou C, Jonas U, Clark CG, Müllen K*, et al.* Viscoelasticity of semifluorinated alkanes at the air/water interface. *Soft Matter* 2011, **7**(17)**:** 7737-7746.

59. Herrmann M, Schneck E, Gutsmann T, Brandenburg K, Tanaka M. Bacterial lipopolysaccharides form physically cross-linked, two-dimensional gels in the presence of divalent cations. *Soft matter* 2015, **11**(30)**:** 6037-6044.

60. Schneider MF, Lim K, Fuller GG, Tanaka M. Rheology of glycocalix model at air/water interface. *Physical Chemistry Chemical Physics* 2002, **4**(10)**:** 1949-1952.

61. Vessely CR, Carpenter JF, Schwartz DK. Calcium-Induced Changes to the Molecular Conformation and Aggregate Structure of β-Casein at the Air−Water Interface. *Biomacromolecules* 2005, **6**(6)**:** 3334-3344.

62. Genzer J, Sivaniah E, Kramer EJ, Wang J, Körner H, Xiang M*, et al.* The orientation of semifluorinated alkanes attached to polymers at the surface of polymer films. *Macromolecules* 2000, **33**(5)**:** 1882-1887.

63. Sollich P, Lequeux F, Hébraud P, Cates ME. Rheology of soft glassy materials. *Physical review letters* 1997, **78**(10)**:** 2020.

64. Kröger M, Vermant J. The Structure and Rheology of Complex Fluids. *Applied Rheology* 2000, **10:** 110-111.

65. Chambon F, Winter HH. Linear viscoelasticity at the gel point of a crosslinking PDMS with imbalanced stoichiometry. *Journal of Rheology* 1987, **31**(8)**:** 683-697.

66. Simons K, Ikonen E. Functional rafts in cell membranes. *nature* 1997, **387**(6633)**:** 569-572.

67. Mammen M, Choi SK, Whitesides GM. Polyvalent interactions in biological systems: implications for design and use of multivalent ligands and inhibitors. *Angewandte Chemie International Edition* 1998, **37**(20)**:** 2754-2794.

68. Dietrich C, Bagatolli L, Volovyk Z, Thompson N, Levi M, Jacobson K*, et al.* Lipid rafts reconstituted in model membranes. *Biophysical journal* 2001, **80**(3)**:** 1417-1428.

69. Oelke J, Pasc A, Wixforth A, Konovalov O, Tanaka M. Highly uniform, strongly correlated fluorinated lipid nanodomains embedded in biological membrane models. *Applied Physics Letters* 2008, **93**(21)**:** 213901.

70. Kaindl T, Oelke J, Pasc A, Kaufmann S, Konovalov O, Funari S*, et al.* Regulation of adhesion behavior of murine macrophage using supported lipid membranes displaying tunable mannose domains. *Journal of Physics: Condensed Matter* 2010, **22**(28)**:** 285102.

71. Quesada-Pérez M, Moncho-Jordá A, Martínez-López F, Hidalgo-Álvarez R. Probing interaction forces in colloidal monolayers: Inversion of structural data. *The Journal of Chemical Physics* 2001, **115**(23)**:** 10897-10902.

72. Yamamoto A, Tanaka H, Toda M, Sotozono C, Hamuro J, Kinoshita S*, et al.* A physical biomarker of the quality of cultured corneal endothelial cells and of the long-term prognosis of corneal restoration in patients. *Nature Biomedical Engineering* 2019, **3**(12)**:** 953-960.

754 73. Verwey EJW. Theory of the stability of lyophobic colloids. *The Journal of Physical*
755 *Chemistry* 1947, **51**(3)**:** 631-636.

756
757 74. Nakahara H, Krafft MP, Shibata O. How self-assembled nanodomains can impact the
758 organization of a phospholipid monolayer. Flower-like arrays. *ChemPhysChem* 2020, **21:**
759 1-6.

760
761 75. East L, Isacke CM. The mannose receptor family. *Biochimica et Biophysica Acta (BBA)-*
762 *General Subjects* 2002, **1572**(2-3)**:** 364-386.

763
764 76. Feinberg H, Jégouzo SA, Lasanajak Y, Smith DF, Drickamer K, Weis WI*, et al.* Structural
765 analysis of carbohydrate binding by the macrophage mannose receptor CD206. *Journal*
766 *of Biological Chemistry* 2021, **296**.

767
768 77. Wixforth A, Strobl C, Gauer C, Toegl A, Scriba J, v. Guttenberg Z. Acoustic manipulation
769 of small droplets. *Analytical and Bioanalytical Chemistry* 2004, **379**(7)**:** 982-991.

770
771 78. Oelke J, Kaindl T, Pasc A, Guttenberg Z, Wixforth A, Tanaka M. Supported Membranes
772 Meet Flat Fluidics: Monitoring Dynamic Cell Adhesion on Pump-Free Microfluidics Chips
773 Functionalized with Supported Membranes Displaying Mannose Domains. *Materials* 2013,
774 **6**(2)**:** 669-681.

775
776 79. Krafft MP, Riess JG. Therapeutic oxygen delivery by perfluorocarbon-based colloids. *Adv*
777 *Colloid Interface Sci* 2021, **294:** 102407.

778
779 80. Krafft M-P, Riess JG. Stable Highly Concentrated Fluorocarbon Gels. *Angewandte*
780 *Chemie International Edition in English* 1994, **33**(10)**:** 1100-1101.

781
782 81. Mielke S, Habe T, Veschgini M, Liu X-H, Yoshikawa K, Krafft MP*, et al.* Emergence of
783 strong nonlinear viscoelastic response of semifluorinated alkane monolayers. *Langmuir*
784 2018, **34:** 2489–2496.

785
786 82. Shi D, Wallyn J, Nguyen D-V, Perton F, Felder-Flesch D, Bégin-Colin S*, et al.*
787 Microbubbles decorated with dendronized magnetic nanoparticles for biomedical imaging.
788 Effective stabilization via fluorous interactions. *Beilstein J Nanotechnol* 2019, **10:** 2103-
789 2115.

790
791 83. Mielke S, Abuillan W, Veschgini M, Liu X, Konovalov O, Krafft MP*, et al.* Influence of
792 Perfluorohexane-Enriched Atmosphere on Viscoelasticity and Structural Order of Self-
793 Assembled Semifluorinated Alkanes at the Air-Water Interface. *ChemPhysChem* 2019,
794 **20**(13)**:** 1698-1705.

795

84. Nguyen PN, Veschgini M, Tanaka M, Waton G, Vandamme T, Krafft MP. Counteracting the inhibitory effect of proteins towards lung surfactant substitutes: a fluorocarbon gas helps displace albumin at the air/water interface. *Chem Commun* 2014, **50:** 11576-11579.

85. Yang G, O'Duill M, Gouverneur V, Krafft MP. Recruitment and immobilization of a fluorinated biomarker across an interfacial phospholipid film using a fluorocarbon gas. *Angew Chem Int Ed* 2015, **54:** 8402-8406.

86. Liu X, Counil C, Shi D, Mendoza-Ortega EE, Vela-Gonzalez AV, Maestro A*, et al.* First quantitative assessment of the adsorption of a fluorocarbon gas on phospholipid monolayers at the air/water interface. *J Colloid Interface Sci* 2021, **593:** 1-10.

87. Workie YA, Kuo C-Y, Riskawati JH, Krathumkhet N, Imae T, Ujihara M*, et al.* Hierarchical composite nanoarchitectonics with a graphitic core, dendrimer and fluorocarbon domains, and a poly(ethylene glycol) shell as O_2 reservoirs for reactive oxygen species production. *ACS Appl Mater Interfaces* 2022, **14:** 35027−35039.

88. Krathumkhet N, Sabrina, Imae T, Krafft MP. Nitric oxide gas in carbon nanohorn/fluorinated dendrimer/ fluorinated poly(ethylene glycol)-based hierarchical nanocomposites as therapeutic nanocarriers. *ACS Appl Bio Mater* 2021, **4:** 2591-2600.

Figure Captions

Figure 1. Self-assembly of lipids with fully hydrogenated and fluorinated chains.
(a) Fully hydrogenated diHC16 forms circular, bubble-like domains. (b) In contrast, partly fluorinated diFC8-8 forms stripe-like domains soon after the surface pressure increases because of corresponding to the coexistence of gas and liquid-expanded phases. The liquid-expanded phase was labeled with fluorescent Texas Red dihexadecyl phosphatidylethanol amine. Partially adapted from Ref. 30.

Figure 2. Shape, size and lateral correlation between mesoscopic domains determined by quantitative grazing incidence small-angle X-ray scattering (GISAXS) analysis at the air/water interface.
(a) Chemical structures of *F*n*H*m diblocks and di(*F*n*H*m) tetrablocks. (b) Experimental setup and scattering geometry. (c) GISAXS signal for the *F*10*H*16 monolayer collected using a two-dimensional detector. The black rectangle is the direct beam masked by a beam stop. The signals in the area surrounded by the white broken line were integrated along q_z. (d) Integrated signal intensity plotted against q_y (circles). The form factor $F(q_y)$ (gray) and structure factor $S(q_y)$ (blue) agreed very well with the experimental data. Partially adapted from Refs. 52 and 53.

Figure 3. Mesoscopic domains of *FnHm* forming a two-dimensional network (gel) even at zero pressure.
(a) Interfacial stress rheometry experimental setup. (b) Typical storage modulus G' and loss modulus G'' is predominantly elastic (G' > G") of the *F*n*H*m monolayer (n = 8, m = 16). The corresponding isotherm shown in the inset indicates that the monolayer under all conditions. (c) Frequency dispersion of the *F*8*H*16 monolayer showed that $G' \propto f^1$ and $G'' \propto f^1$ at π = 0 mN/m, which is a characteristic of soft glassy matter. At $\pi > 0$, the power law exponents change to those of Kelvin–Voigt solid, $G' \propto f^0$ and $G'' \propto f^1$. (d) Plot of G'' against G' for the *F*8*H*16 monolayer acquired at different f values. The inset is the phase angle δ plotted against the frequency, indicating that the monolayer is predominantly elastic over the whole frequency window at π = 0 mN/m (G" < G') and the phase shift δ remains constant at ≈ 0.6. Adapted from Ref. 56.

Figure 4. Perfluorinated lipid (FLn) achieving long-range order in a phospholipid membrane. (a) Chemical structure of FLn lipids (n = 10, 13, 17). (b) Fluorescence microscopy images of FL10, FL13, and FL17 measured at π = 20 mN/m at molar fractions χ of 0.10, 0.20, and 0.33. The brght regions coincide with DOPC (matrix) lipids, while the dark regions are FLn domains. (c) Equilibrium domain sizes D_{eq} calculated using the effective dipole model (T) and experimental data (E) for χ = 0.33. The size distributions (mean ± standard deviation) and the errors of parameters used for the calculation are presented by the error bars. (d) Normalized potential of mean force $-V(r)/k_BT$ plotted against distance from the center of domain r. Adapted from Refs. 69 and 70.

Figure 5. Highly ordered biofunctional domains used as biomimetic coating materials. (a) Chemical structure of FL10 coupled to mannose (FL10Man). (b) Normalized potential of mean force and fluorescence image of FL10Man indicating the dominant role of dipole repulsion in the formation of highly ordered domains. (c) Membrane with FL10Man domains used as a biomimetic coating material for cells. Adhesion of a macrophage cell on a pure phospholipid membrane (left), pure FL10Man membrane (middle), and membrane incorporating FL10Man at χ = 0.33 (right). The cells form discrete contact points on the FL10Man domains. (d) Integration of FL10Man-incorporating membranes into coverless microfluidics driven by a surface acoustic wave (SAW) to investigate cell adhesion under high shear stress. (e) Cell-sized leukocyte model coated with sialyl-LewisX antigen microdomains. Adapted from Refs. 29, 70, and 78.

Figure 6. Hierarchically organized fluorinated self-assemblies for biomedical applications. (a) Fluorocarbon-stabilized microbubbles with a coating of phospholipids and dendronized iron oxide nanoparticles for bimodal ultrasound/MRI imaging diagnostics. Adapted from Ref. 73. (b) Left: the fluorocarbon saturating the inner gas content of the microbubble allows adsorption of the fluorinated hypoxia biomarker EF5 in a monolayer of phospholipids. Right: Optical microscopy image of an aqueous dispersion of EF5-containing microbubbles. Adapted from Ref. 76. (c) Schematic representation of the functionalization of a graphene oxide (GO) sheet by a layer of fluorinated dendrimers (*F*-DEN) on which a layer of fluorinated PEG (*F*-PEG) is adsorbed. These nanocomposites have proved efficacy as O_2 reservoirs for reactive oxygen species production to kill bacteria and perform photodynamic therapy. Adapted from Ref. 87.

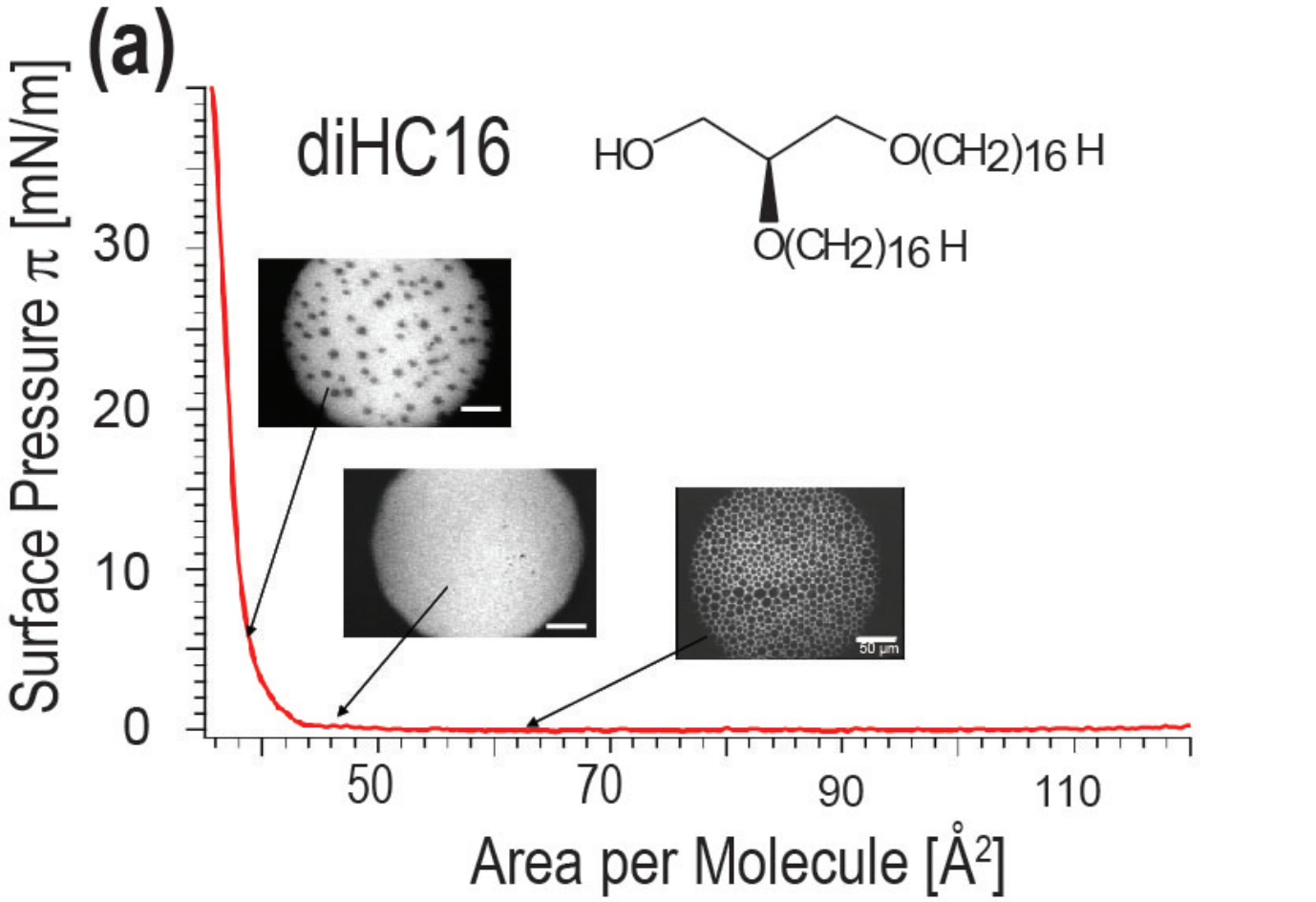
(a)
diHC16
HO
O(CH2)16 H
O(CH2)16 H
Surface Pressure π [mN/m]
0
10
20
30
50
70
90
110
Area per Molecule [Å²]
50 µm

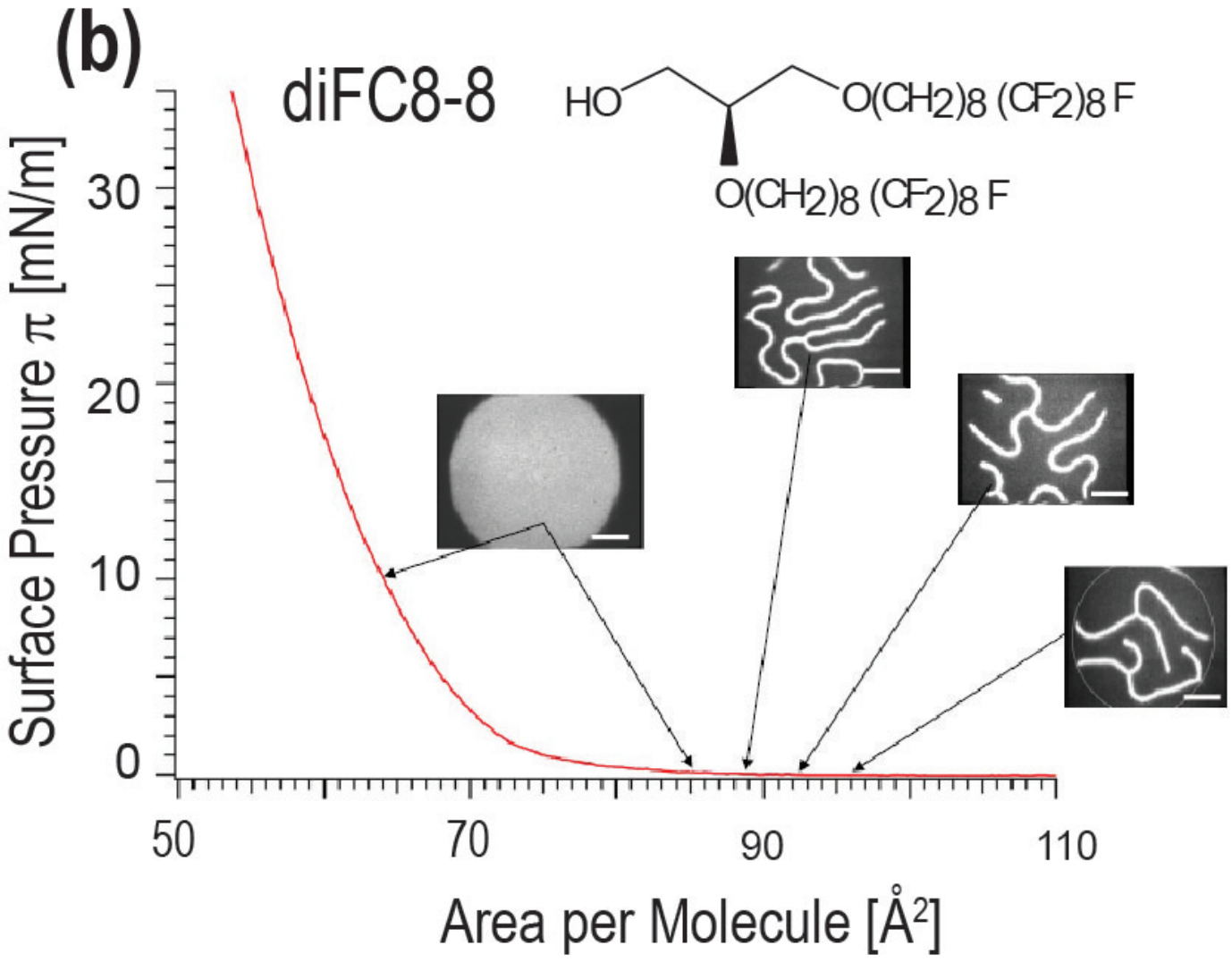
(b)
diFC8-8
HO
O(CH2)8 (CF2)8 F
O(CH2)8 (CF2)8 F
Surface Pressure π [mN/m]
0
10
20
30
50
70
90
110
Area per Molecule [Å²]

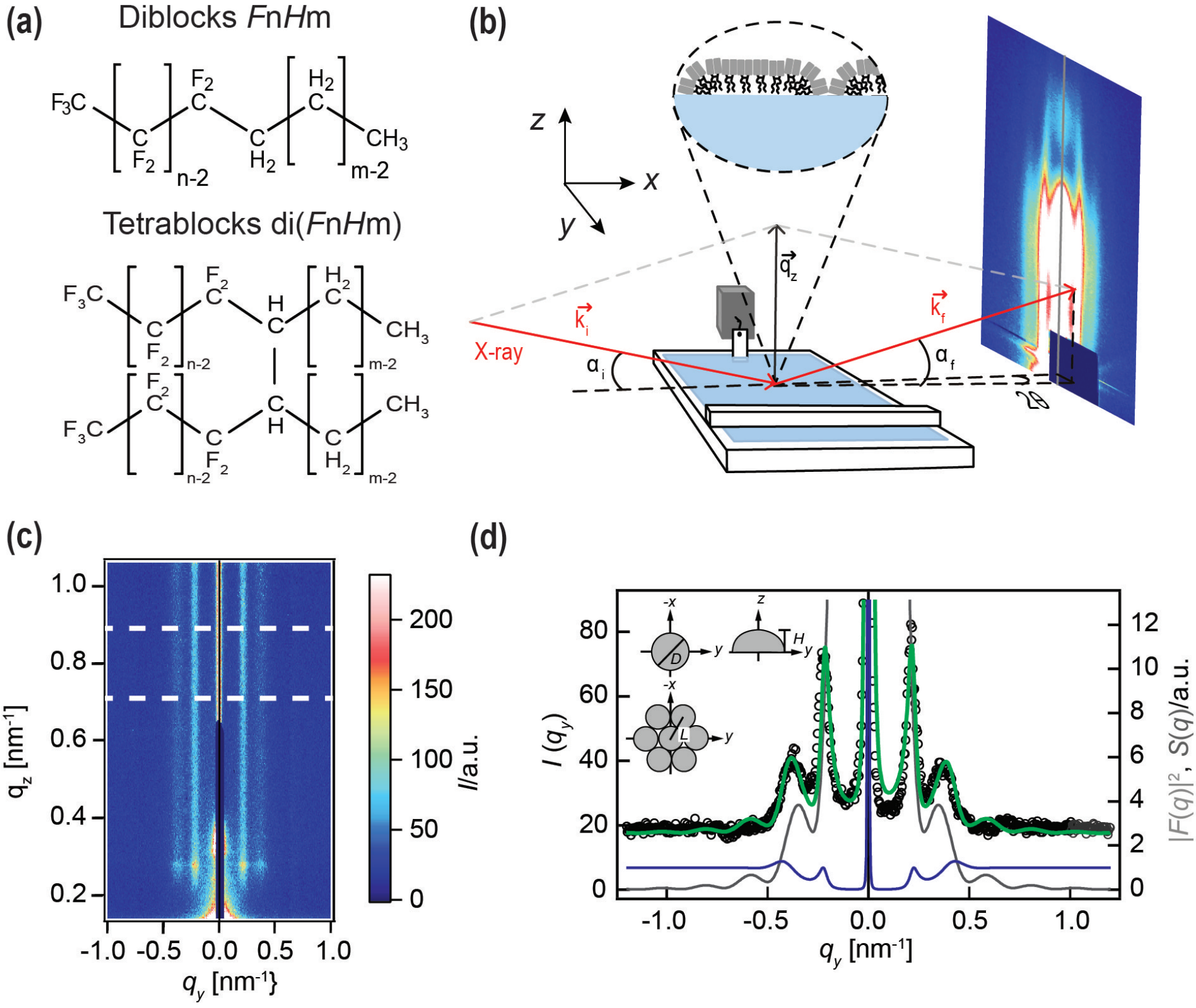
(a)
Diblocks FnHm
F3C
F2
C
H2
C
CH3
C
F2
C
H2
n-2
m-2
Tetrablocks di(FnHm)
F3C
F2
C
H
C
H2
C
CH3
C
F2
C
H
C
H2
n-2
m-2
(b)
z
x
y
q_z
k_i
k_f
X-ray
α_i
α_f
2θ
(c)
q_z [nm^-1]
1.0
0.8
0.6
0.4
0.2
-1.0 -0.5 0.0 0.5 1.0
q_y [nm^-1]
200
150
100
50
0
I/a.u.
(d)
I (q_y)
80
60
40
20
0
-1.0 -0.5 0.0 0.5 1.0
q_y [nm^-1]
12
10
8
6
4
2
0
|F(q)|^2, S(q)/a.u.
-x
z
y
D
H
L

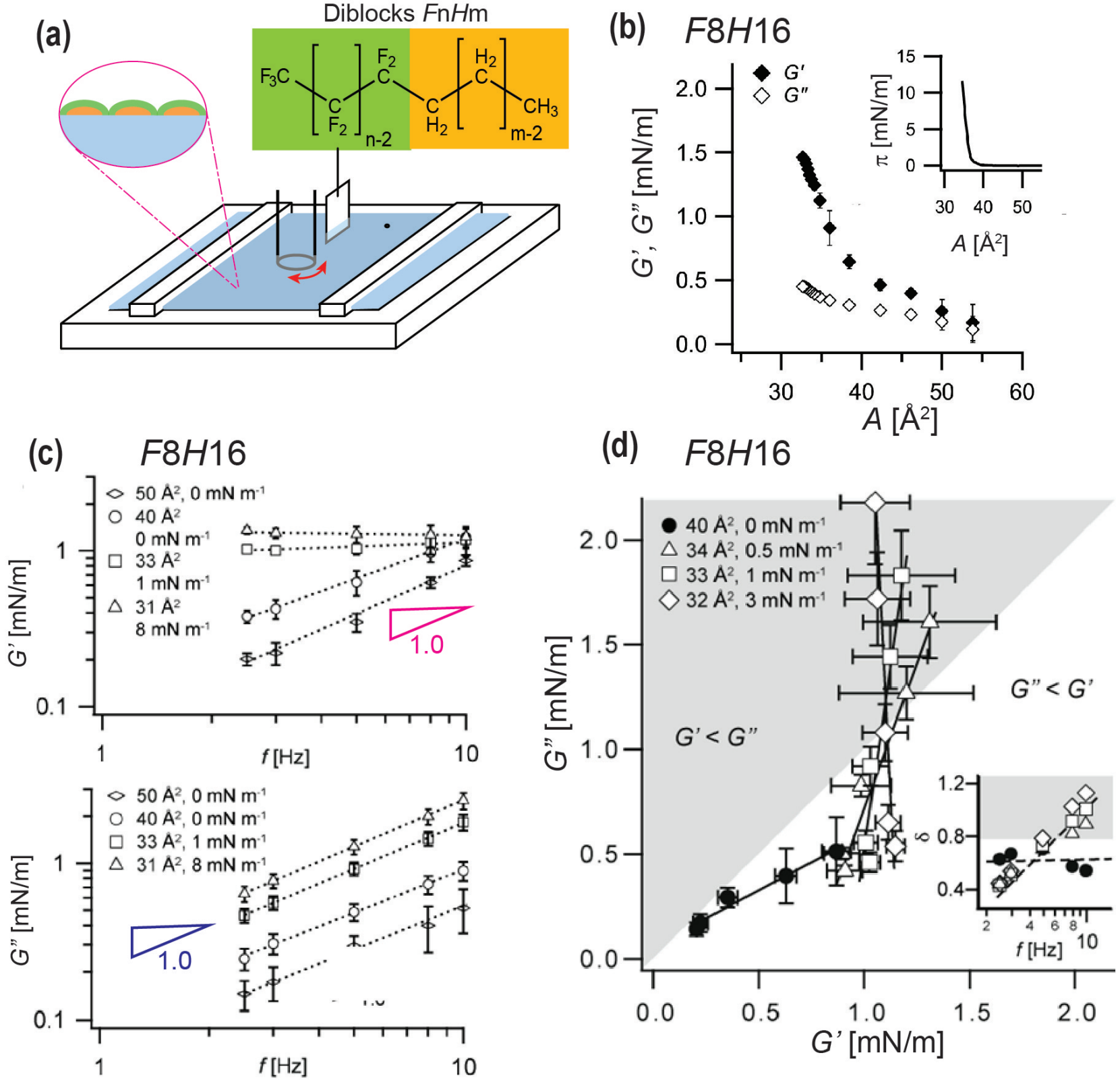
(a)
Diblocks FnHm
F3C
F2
C
F2
n-2
H2
C
H2
CH3
m-2
(b)
F8H16
G′
G″
G′, G″ [mN/m]
A [Å2]
π [mN/m]
(c)
F8H16
50 Å2, 0 mN m-1
40 Å2
0 mN m-1
33 Å2
1 mN m-1
31 Å2
8 mN m-1
G′ [mN/m]
f [Hz]
1.0
G″ [mN/m]
(d)
F8H16
40 Å2, 0 mN m-1
34 Å2, 0.5 mN m-1
33 Å2, 1 mN m-1
32 Å2, 3 mN m-1
G′ < G″
G″ < G′
G″ [mN/m]
G′ [mN/m]
δ
f [Hz]

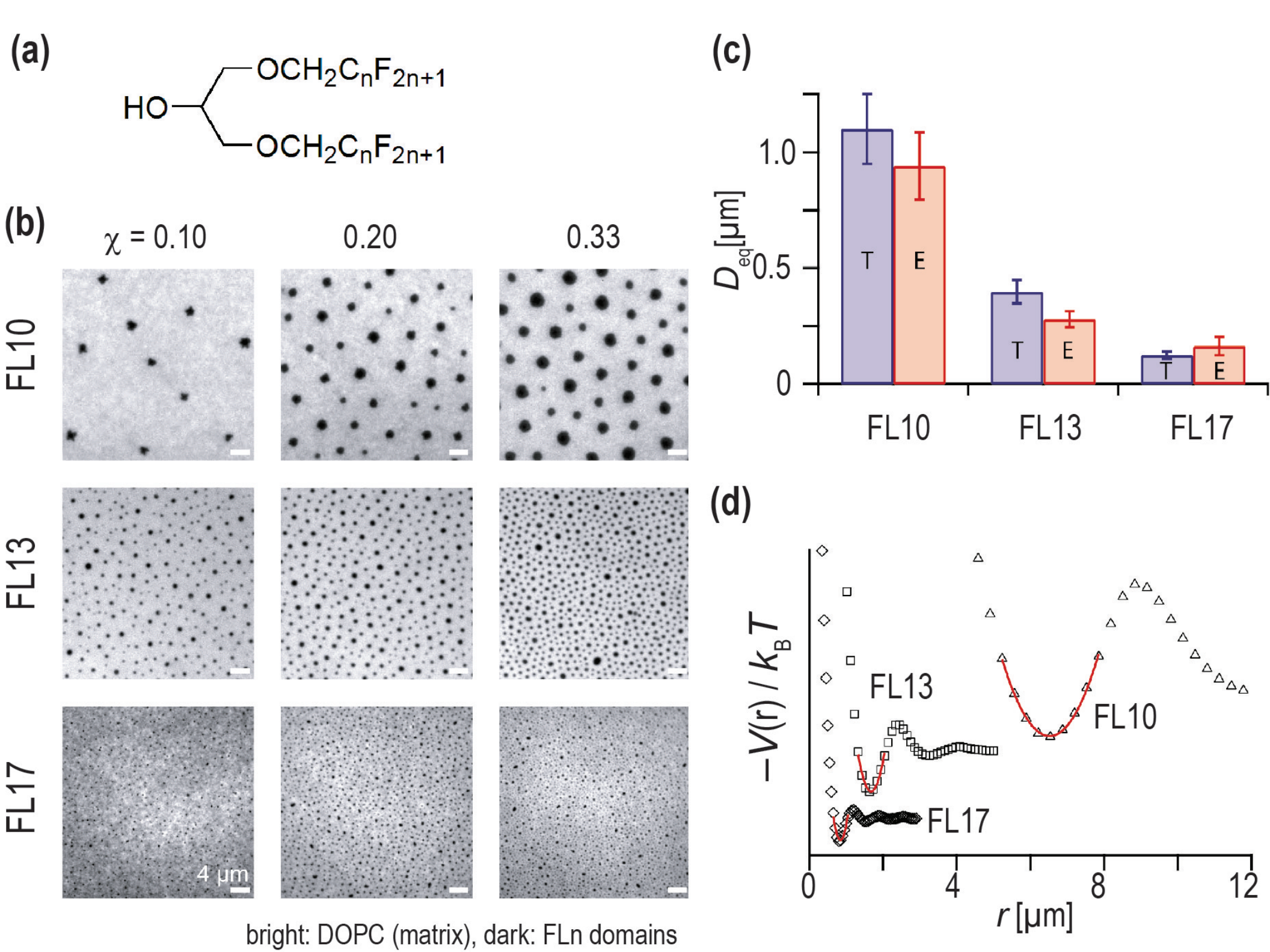
(a)
HO
$OCH_2C_nF_{2n+1}$
$OCH_2C_nF_{2n+1}$
(b)
χ = 0.10
0.20
0.33
FL10
FL13
FL17
4 μm
bright: DOPC (matrix), dark: FLn domains
(c)
D_{eq}[μm]
1.0
0.5
0
T
E
FL10
FL13
FL17
(d)
$-V(r) / k_B T$
FL13
FL10
FL17
0
4
8
12
r [μm]

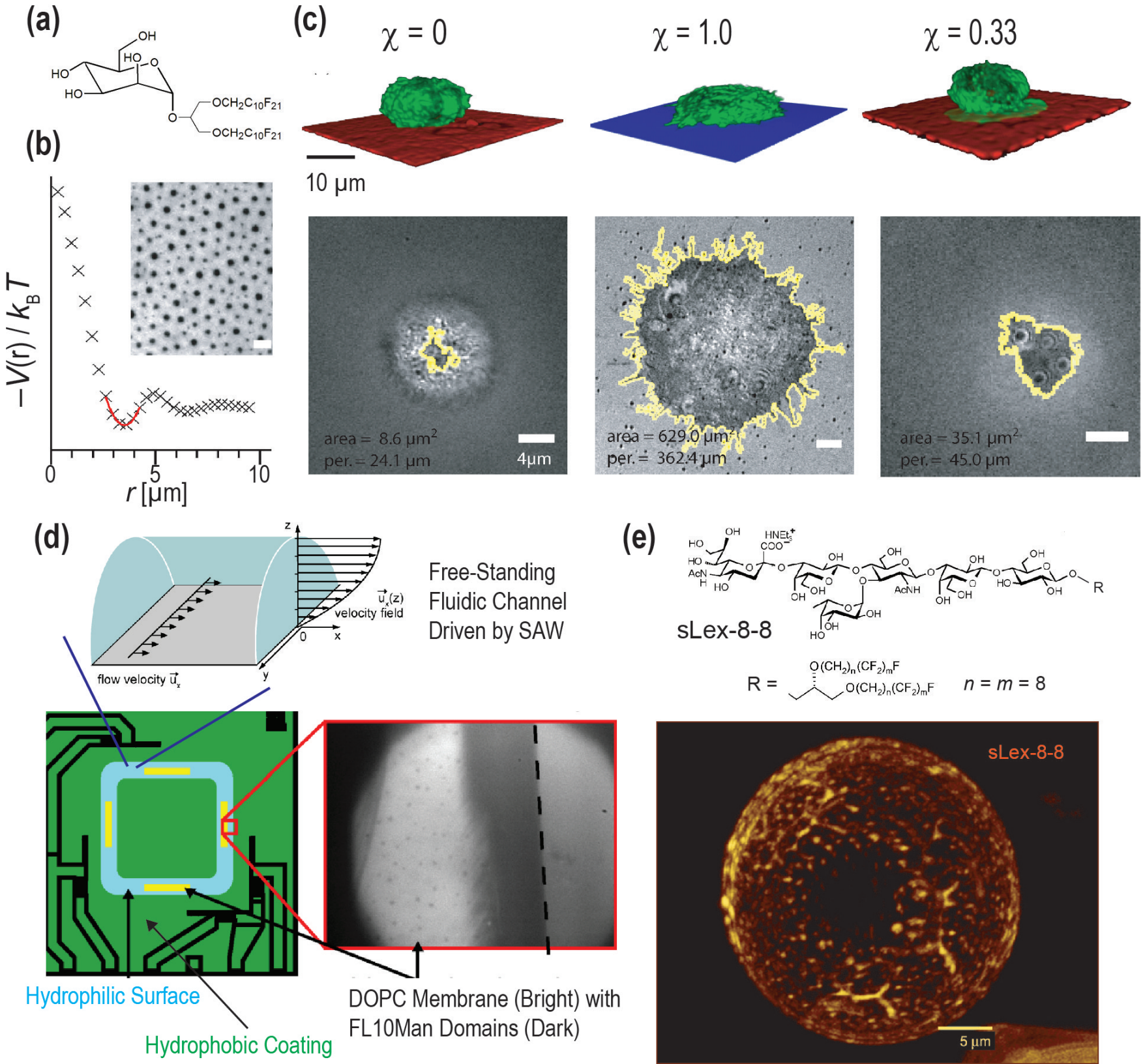
(a)
OH
HO
HO
HO
O
OCH2C10F21
OCH2C10F21
(b)
−V(r) / kBT
0
5
10
r [μm]
(c)
χ = 0
χ = 1.0
χ = 0.33
10 μm
area = 8.6 μm2
per. = 24.1 μm
4μm
area = 629.0 μm2
per. = 362.4 μm
area = 35.1 μm2
per. = 45.0 μm
(d)
z
x
y
0
velocity field
flow velocity
Free-Standing
Fluidic Channel
Driven by SAW
Hydrophilic Surface
Hydrophobic Coating
DOPC Membrane (Bright) with
FL10Man Domains (Dark)
(e)
HNEt3+
COO−
AcNH
R
sLex-8-8
R =
O(CH2)n(CF2)mF
n = m = 8
sLex-8-8
5 μm

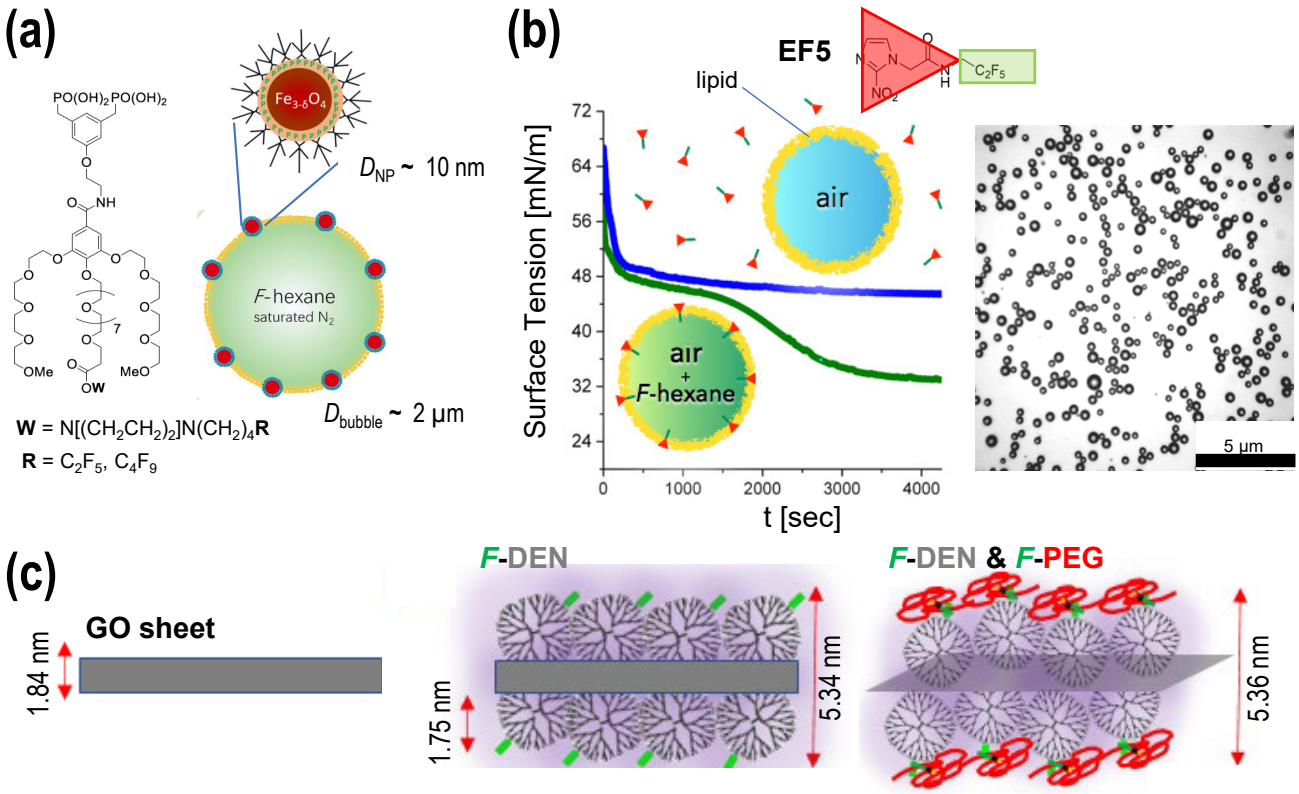
(a)
PO(OH)2PO(OH)2
NH
OMe
MeO
OW
7
Fe3-δO4
F-hexane
saturated N2
DNP ~ 10 nm
Dbubble ~ 2 μm
W = N[(CH2CH2)2]N(CH2)4R
R = C2F5, C4F9
(b)
EF5
lipid
air
air
+
F-hexane
Surface Tension [mN/m]
72
64
56
48
40
32
24
0
1000
2000
3000
4000
t [sec]
5 μm
(c)
GO sheet
1.84 nm
F-DEN
1.75 nm
5.34 nm
F-DEN & F-PEG
5.36 nm